Simulating the impact damage of laminated glass considering mixed mode delamination using FEM/DEM

Wang, Xing-er; Yang, Jian; Wang, Feiliang; Liu, Qingfeng; Xu, Han

DOI:
10.1016/j.compstruct.2018.05.127

Document Version
Peer reviewed version

Citation for published version (Harvard):
Wang, X, Yang, J, Wang, F, Liu, Q & Xu, H 2018, 'Simulating the impact damage of laminated glass considering mixed mode delamination using FEM/DEM', *Composite Structures*.
https://doi.org/10.1016/j.compstruct.2018.05.127

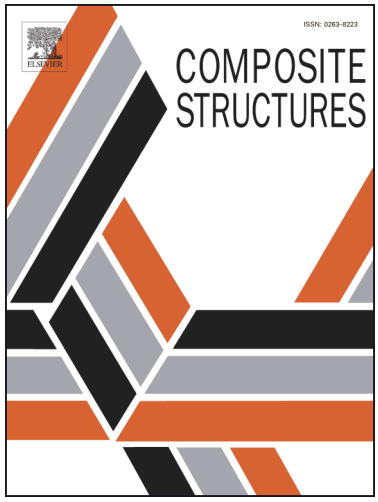

Simulating the impact damage of laminated glass considering mixed mode delamination using FEM/DEM

Xing-er Wang, Jian Yang, Feiliang Wang, Qingfeng Liu, Han Xu

PII: S0263-8223(18)30230-7
DOI: https://doi.org/10.1016/j.compstruct.2018.05.127
Reference: COST 9766

To appear in: *Composite Structures*

Received Date: 15 January 2018
Revised Date: 22 April 2018
Accepted Date: 28 May 2018

Please cite this article as: Wang, X-e., Yang, J., Wang, F., Liu, Q., Xu, H., Simulating the impact damage of laminated glass considering mixed mode delamination using FEM/DEM, *Composite Structures* (2018), doi: https://doi.org/10.1016/j.compstruct.2018.05.127

Simulating the impact damage of laminated glass considering mixed mode delamination using FEM/DEM

Xing-er Wang[a], Jian Yang[a,b], Feiliang Wang[a], Qingfeng Liu[a], Han Xu[a]

[a] State Key Laboratory of Ocean Engineering, Shanghai Jiao Tong University, Shanghai 200240, PR China

[a] School of Naval Architecture, Ocean and Civil Engineering, Shanghai Jiao Tong University, Shanghai 200240, PR China

[a] Collaborative Innovation Center for Advanced Ship and Deep-Sea Exploration (CISSE), Shanghai 200240, P.R. China

[b] School of Civil Engineering, University of Birmingham, Birmingham B15 2TT, UK

Abstract: This paper presents an approach for modelling the impact breakage of the laminated glass (LG) using the combined finite-discrete element method (FEM/DEM). It encompasses the discrete crack model for glass, the Mooney-Rivlin model to represent the hyperelasticity of the PVB interlayers. The improved Xu and Needleman model is adapted to serve as the mixed-mode interfacial constitutive law, in particular, describing the combined damage-plasticity behaviour for irreversible unloading and thus can predict the interlaminar cohesion failure. The comparison between the simulation and the experimental results for several laminated glass make-ups shows that this interfacial model can adequately reproduce the typical delamination behaviour. The characteristics of the stress wave propagation and the interlayer tearing in the example cases can be satisfactorily reproduced. The shortcoming of the discrete crack model in modelling the impact damage of strengthened glass and the resulting errors are discussed as well.

Keywords: Impact fracture; Combined finite discrete element method; Mixed-mode delamination; Cohesive zone model; laminated glass

1 Introduction

Monolithic glass under the impact load exhibits an extremely brittle failure nature without showing any obvious early indications of yield or hardening, thus causing tremendous risks during service [1-3]. In order to mitigate such risks, the laminated glass (LG) that comprises two or more glass layers with interlayers is introduced to improve the post-breakage strength without losing the favorable transparency feature that the glass possesses. Being a type of composite structure, a typical laminated glass panel often exhibits the following force-displacement behavior (see **Fig. 1**) when subjected to out-of-plane loading. It can be subdivided into five typical phases [4]:

(1) All glass layers behave elastically and the force and displacement relation remains linear as indicated by phase 1 in **Fig. 1**.

(2) The first glass layer breaks while the others remain intact, which will cause a sudden drop in force but the remaining layers can continue to withstand load (see phase 2).

(3) The rest of glass layers break as well yielding a second drop in the force-displacement curve. The interlayers start to carry the load but still perform elastically (phase 3).

(4) The broken glass pieces are hold together in compression and interlayer will act in tension. Interlayer starts to behave plastically (phase 4).

(5) At point 5, interlayer fails once meeting the failure criterion, i.e., pierced by the debris or experienced tearing failure in tension.

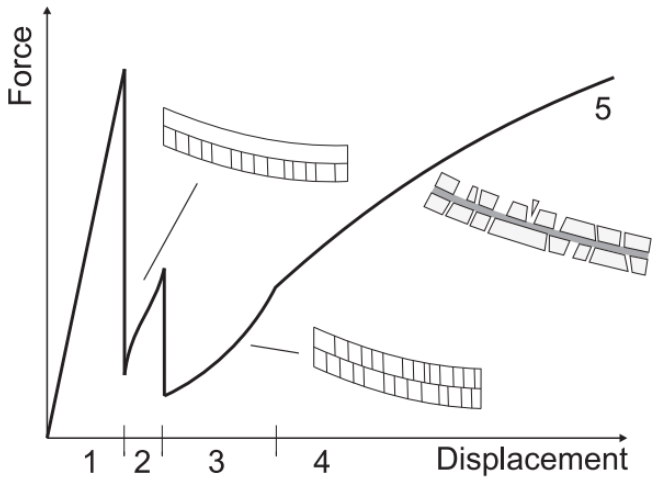

Fig. 1. Schematic failure of laminated glass.

Phases 2-5 represent the post breakage stage, where the LG panels retain their load bearing capacity before the interlayer fails. In the late stage, e.g. phase 4, the membrane action may be noticed if adequate restraining effect are imposed at the edges of LG panel. The loading capacity due to the membrane action can be higher than the pre-breakage stage in phase 1 [5]. The behavior in the post breakage stage has attracted growing interests in the structural use of laminated glass.

In order to examine the failure mechanisms under different loading conditions that are difficult to implement in lab tests, numerical methods turn out to be a useful tool for simulating the post breakage behaviour of laminated glass. A suitable model should be formulated to resemble the loading behaviour of such composite material both before and after breakage, and must capture the transition state from continuity to discontinuity. The finite element method (FEM) and the discrete element method (DEM) have been commonly employed in previous studies [6-8] to this end. A variety of constitutive models and failure criterions have been incorporated to simulate the glass fracturing in FEM. For example, the continuum damage mechanics (CDM) based constitutive models [9, 10], combined with the fracture criterion determined by the principal stress and von Mises stress [5] or critical energy threshold approach [11], were developed to capture the crack initiation. The failed element erosion strategy [12, 13], where the residual strength of glass fragment is ignored based on the assumption that the failed elements will not influence the subsequent fracture, was commonly used to simulate the fracture evolution after meeting the failure criterion. It has been demonstrated that FEM is reliable in predicting the pre-breakage and the crack initiation. However it is found that FEM often experiences significant difficulties to simulate problems such as large deformations and strong discontinuity in the post breakage stage.

DEM was originally invented to simulate granular media, and then extended to solving continuum problems by developing bonded particle models [14]. There are fewer DEM applications in modelling glass failure, comparing to FEM. Most of them focus on developing novel contact model, e.g., the nonlinear springs between particles to match the global response by calibrating its contact parameters. Tokunaga et al. [15] proposed two kinds of nonlinear springs, the pore-spring and the element-spring, to account for the mechanical interaction inside thermally tempered glass. A three dimensional beam model combined with a failure criterion based on the

equivalent hydrostatic stress was introduced to tackle the phenomenon of the typical hertzian cone crack using an indentation test [16]. Zang [17] established a 3D discrete element model for LG panels by employing the Mohr-Coulomb failure criterion to predict the crack initiation. The effect of strain rate on mechanical property of the polyvinyl butyral (PVB) interlayer was also considered. DEM has been shown to be capable of handling strong discontinuity problems in the post breakage stage [18]. However the sensitivity of the parameter calibration in the contact model will lead to a higher degree of unpredictability of its global behaviour, causing low reliability in obtaining the crack pattern [6].

In order to couple the advantages of both FEM and DEM in simulating the impact damage of LG panel, the combined finite-discrete element method (FEM/DEM) [19] was introduced recently. It discretises the target object with discrete elements, and inserts cohesive elements between adjacent element pairs. The crack propagation coincides with the failure of cohesive elements. FEM/DEM is reliable in predicting both the pre-breakage and the crack pattern of monolithic glass in plane stress condition [6, 20]. Munjiza [21] developed a fracture model for multi-layered thin shells and successfully captured the radial and circumferential cracks in post breakage stage of flat glass panel, showing its potential to model the complex fracture of laminated glass.

To develop an approach of FEM/DEM to simulate the post breakage of laminated glass, two important aspects should be considered, i.e., the large deformation of interlayer with glass fragment attached, and the delamination behaviour of the interface between glass and interlayer. The former relates to the formation of the membrane action, and the latter affects its post-breakage strength [22, 23]. The delamination failure is primarily caused by the interfacial shear and peeling stresses, the coupling of which will create a mixed fracture mode consisting of both Modes I and II. However, either the existing fracture model of FEM/DEM or the combined single and smeared crack model [24] is proposed for Mode I condition only as such it will not be able to simulate the mixed-mode delamination behaviour of the glass-interlay interface after phase 3. To date, no attempts have been seen to capture the delamination process in FEM/DEM modelling.

In this work, an algorithm combining both the constitutive laws for interlayer material and the mixed-mode interfacial behavior is devised for simulating the LG failure. The interfacial model concerns the unloading behavior using the combined damage and plastic model. In the

present model, a Mooney-Rivlin model is adopted for the hyperelasticity behavior of PVB interlayer. The modified Xu and Needleman model is used to simulate the combined damage-plastic behavior during interface delamination. LG beam examples containing several glass make-ups and subjected to the hard body impact is modelled. Through a comparison study of the FEM/DEM simulation and the impact experiment, the model proposed is evaluated by identifying both its advantages and the shortcomings. The corresponding errors are revealed and discussed as well.

2 Modelling Methodology

2.1 Combined finite-discrete element method

FEM/DEM is an innovative numerical method proposed to analyse the deformation and stress of discrete elements through the standard continuum finite element formulation with a transient algorithm, and by processing the contacts and motion of elements based on DEM.

The computational object is discretised into separate bodies, but can be represented as a deformable continuum, and between them zero-thickness cohesive joint elements are inserted. Cohesive zone models can be employed in the cohesive elements to describe the fracture or decohesion behaviour of material. Thus, the transition from continuity to discontinuity is captured when the cohesive joint elements break.

In order to optimize the contact detection following the breakage occurrence, FEM/DEM develops a high efficient approach, i.e., no binary search (NBS) algorithm [25], of which the total detection time is proportional to N (N is the total number of discrete elements). Once detecting the contact of elements, a potential function based method [26] will be employed to yield a realistic distribution of contact forces. It assumes the penetration of any differential area dA of contactor β_c into the target β_t, where the subscript *c* and *t* denote the contactor and the target, respectively (**Fig. 2**), will induce a differential contact force given by:

$$\mathrm{d}\mathbf{f}_c = p_n[\mathrm{grad}\varphi_c(P_c) - \mathrm{grad}\varphi_t(P_t)]\mathrm{d}A \tag{1}$$

where φ_c and φ_t are potential function for contactor and target elements, respectively; p_n represents the normal penalty parameter. The differential contact force $\mathrm{d}\mathbf{f}_c$ due to differential

overlap $\mathrm{d}A$ is defined by overlapping point belonging to contactor P_c and target P_t. Thus, the total contact force can be obtained by integrating over the overlapping area *S*.

$$\mathbf{f}_c = \int_{S=\beta_c \cap \beta_t} p_n [\mathrm{grad}\varphi_c(P_c) - \mathrm{grad}\varphi_t(P_t)] dA \tag{2}$$

It can be rewritten as an integral over the boundary of the overlapping area Γ using the Green's theorem

$$\mathbf{f}_c = \oint_{\Gamma_{\beta_c \cap \beta_t}} p_n \boldsymbol{n}_\Gamma (\varphi_c - \varphi_t) d\,\Gamma \tag{3}$$

where $\boldsymbol{n}_\Gamma$ is the outward unit normal to the boundary of the overlapping area.

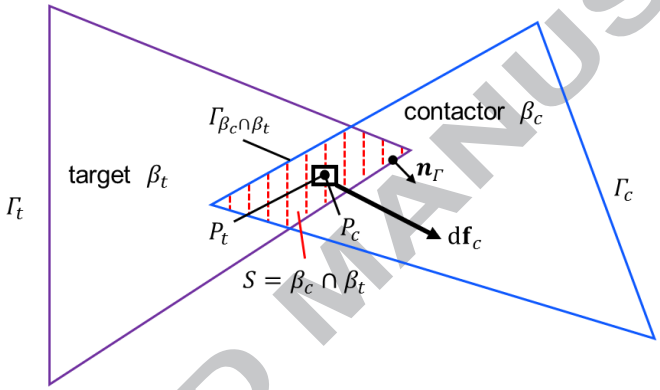

Fig. 2. Contact force on differential overlap around points P_c and P_t.

Through such procedure, the contact detection and interaction of elements can be managed when the following motion of separate bodies are computed according to Newton's second law. The interaction forces of the elements in contact are calculated using a penalty function, in which the penalty terms will govern the level of penetration in FEM/DEM. The penalty terms are selected according to Mahabadi's work [27], which has suggested that penalties can be taken as the multiples of Young's modulus *E*. The chosen penalties in this work are *E* for the contact penalty, 10*E* for tangential penalty, 10*E* for fracture penalty, respectively.

2.3 Constitutive law of polyvinyl butyral interlayer

PVB is commonly used as interlayer in the manufacture of laminated glass. It exhibits the capability of fully recovering without significant plastic deformation after being released from extending by several times of its original size. Mooney-Rivlin model is demonstrated to be suitable to describe the hyperelasticity of PVB both in the compression [28] and tension [29].

Since only elastic and strain softening based elements are available in FEM/DEM, the Mooney-Rivlin constitutive model is implemented to model the PVB interlayer.

Suppose the material is subjected to a displacement field **u**, the deformation gradient $\bar{\mathbf{F}}$ and its Jacobian are defined as:

$$\bar{\mathbf{F}} = \mathbf{I} + \frac{\partial \mathbf{u}}{\partial \mathbf{X}};\ J = \det \bar{\mathbf{F}} \tag{4}$$

where **I** is the identity tensor, **X** is the reference position vector, *J* represents the total volume change. The left Green strain tensor can be computed by

$$\mathbf{B} = \bar{\mathbf{F}} \cdot \bar{\mathbf{F}}^{\mathrm{T}} \tag{5}$$

An adapted Mooney-Rivlin model [30] being employed, the strain energy function is given in terms of three input constants:

$$\bar{U}(\bar{I}_1, \bar{I}_2, \bar{I}_3) = \bar{U}(\bar{I}_1, \bar{I}_2, J) = \frac{\mu_1}{2}(\bar{I}_1 - 3) + \frac{\mu_2}{2}(\bar{I}_2 - 3) + \frac{K_1}{2}(J-1)^2 \tag{6}$$

where μ_1, μ_2 and K_1 are material properties, which can be related to the shear modulus μ_s and bulk modulus *K* of the interlayer by two equations, i.e. $\mu_s = \mu_1 + \mu_2$ and $K = K_1$, under small deformation. These properties can be obtained through performing material tests, e.g., the simple or equibiaxial tension, pure shear and volumetric compression. $\bar{I}_1 = \mathbf{I} : \mathbf{B}$, $\bar{I}_2 = \frac{1}{2}(\bar{I}_1{}^2 - \frac{\mathbf{B}:\mathbf{B}}{J^{4/3}})$ and $\bar{I}_3 = \det \mathbf{B} = J^2$ are an alternative set of invariants of **B**, being more convenient for nearly incompressible material.

The second Piola-Kirchhoff stress can be written by differentiating the strain energy function $\bar{U}$ with respect to the left Green strain tensor **B**

$$\mathbf{S} = 2\frac{\partial \bar{U}}{\partial \mathbf{B}} = 2\frac{\partial \bar{U}}{\partial \bar{I}_1}\mathbf{I} + 2\frac{\partial \bar{U}}{\partial \bar{I}_2}\left(\bar{I}_1\mathbf{I} - \frac{\mathbf{B}}{J^{4/3}}\right) + 2\frac{\partial \bar{U}}{\partial \bar{I}_3}J^2\mathbf{B}^{-1} \tag{7}$$

The Cauchy stress tensor is given as

$$\mathbf{T} = J^{-1}\bar{\mathbf{F}}\mathbf{S}\bar{\mathbf{F}}^{\mathrm{T}} \tag{8}$$

The stress strain relationship of PVB interlayer is computed using Eqs. (7) and (8). The interlayer tearing occurs when its maximum principal stress exceeds its failure stress.

In this work, the constants in Mooney-Rivlin model are determined based on Yang's experimental data [29] of PVB material at different strain rates. Because the impact cases in this work are of low impact velocity and the corresponding strain rate is nearly 10^2 s^{-1}, the data recorded at strain rate being 125.6 s^{-1} are adopted for the data fitting. The constants in **Eq. (6)** are

then determined as follows: μ_1 = 5.212 MPa, μ_2 = -3.264 MPa and K_1 = 20 MPa. To calibrate the Mooney-Rivlin model implemented in FEM/DEM, a simple uniaxial test of PVB material is simulated. The simulated stress strain result is compared with experimental data as shown in **Fig. 3**, it can be seen that the developed model can adequately model the typical constitutive behavior of PVB interlayer.

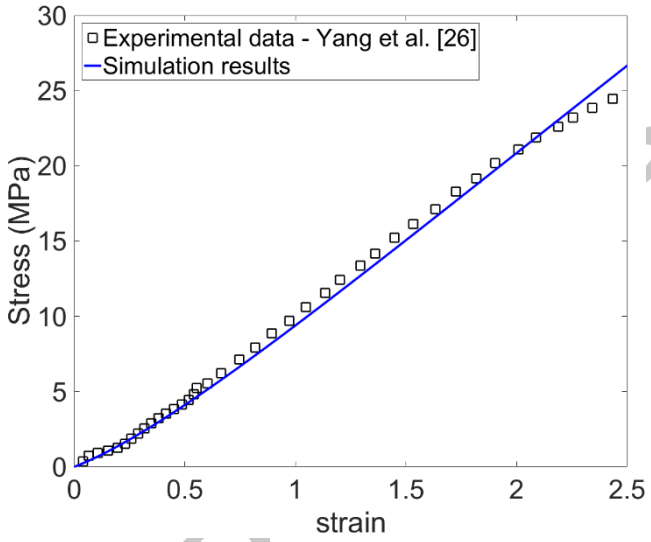

Fig. 3. Stress-strain law of PVB material used in the FEM/DEM simulation.

2.4 Mixed-mode delamination of laminated glass

Allowing for the delamination between glass and interlayer is of importance to the post breakage performance of laminated glass, because it can facilitate the absorption of impact energy by viscoelastic or plastic deformation of interlayer. The occurrence of delamination can also reduce the tendency of tearing of the interlayer that undergoes severe deformation at the crack location, thus to avoid the rapid penetration of objects. The bonding interface is subjected to the mixed-mode loading, i.e., tension and shear, when glass panel is under the out of plane impact. However, the interfacial constitutive law for mixed mode can be rarely found in existing numerical investigations of laminated glass. The commonly used model is the simplified bilinear separation-traction [31, 32]. In the event of the failure of cohesive joints between the discrete elements, the use of cohesive zone model (CZM) in FEM/DEM is viable to describe the crack initiation and propagation for material that fractures. In this work, a cohesive zone model based on

the improved Xu and Needleman model [33] is adopted to model the cohesion failure considering irreversible unloading.

Combined damage-plasticity unloading

Several recent work for the mixed-mode CZMs [34] shows that the improved Xu and Needleman model is capable of producing satisfactory consistency on the interfacial failure. Therefore, this model is selected for incorporating the combined damage-plasticity behaviors (**Fig. 4**) in this study. This is due to the observations from the real decohesion process suggesting that the interface often exhibits a delamination mechanism featured as a combination of damage and plasticity. This mechanism will result in an unloading and reloading behavior shifting from the full damage to the full plasticity. The combined damage-plasticity behavior is divided into three phases in this work, which are 1) exponential loading; 2) fully elasto-plasticity unloading-reloading; 3) combined damage and plasticity unloading-reloading.

The total opening can be seen as the sum of the plastic opening and the elastic opening, i.e. $o = o_p + o_e$. The elastic separation o_e can be obtained through the cohesive zone law, and the total opening can be calculated by the coordinates of the joint elements.

In Phase 1, by introducing a damage index and a coupled term, the cohesive zone law in the first phase follows the exponential form without unloading and is given by **Eqs. (9)** and **(10)**.

$$\text{Normal traction: } T_n = K_{n0}(1 - d_n\langle o\rangle)(1 - d_{c,t}\langle o\rangle)o \tag{9}$$

$$\text{Tangential traction } T_t = K_{t0}(1 - d_t)(1 - d_{c,n})s \tag{10}$$

where the Macauley operator $\langle\cdot\rangle$ implies that mixed mode delamination is unavailable when the negative normal relative opening occurs. d_i and $d_{c,i}$ (i = n or t) represent the damage index and the coupled term respectively, and can be written as:

$$d_n = 1 - \exp\left(-\frac{o_{max}}{o_p}\right),\ d_{c,n} = 1 - \exp\left(-\frac{o_{max}}{o_p}\right)\left(1 + \frac{o_{max}}{o_p}\right) \tag{11}$$

$$d_t = d_{c,t} = 1 - \exp\left(-\frac{s_{max}^2}{2s_p^2}\right) \tag{12}$$

where o_{max} and s_{max} denote the maximum opening and separation in the prior loading history, respectively, before the cohesive joints fail. An intrinsic model is used here with the characteristic lengths are given by:

$$o_p = \frac{G_{IC}}{f_t \exp(1)},\ s_p = \frac{G_{IIC}}{f_s\sqrt{1/2\exp(1)}} \tag{13}$$

where G_{IC}, G_{IIC} are the Mode I and Mode II critical fracture energy respectively. f_s and f_t are the bonding strength in the normal and tangential directions, respectively. K_{i0} (i = n or t) is the initial stiffness of the cohesive zone as follows:

$$K_{n0} = \frac{\partial T_n}{\partial o}\Big|_{o=0,s=0} = \frac{G_{IC}}{o_p^2},\ K_{t0} = \frac{\partial T_t}{\partial s}\Big|_{o=0,s=0} = \frac{G_{IIC}}{s_p^2} \tag{14}$$

In Phases 2 and 3, the plastic limits in the normal and tangential directions, o_{pl} and s_{pl}, are introduced as the critical parameters indicating the unloading-reloading phases. The unloading traction in these two phases can be written as:

$$\text{Normal traction: } T_n = K_{n0}(1 - d_n\langle o_e\rangle)(1 - d_{c,t}\langle o_e\rangle)o_e \tag{15}$$

$$\text{Tangential traction } T_t = K_{t0}(1 - d_t)(1 - d_{c,n})s_e \tag{16}$$

where $d_{c,t}$ and $d_{c,n}$ are the coupled degradation terms given by **Eqs. (11)** and **(12)**. o_e and s_e represent the elastic separation in the normal and tangential directions, respectively. The effective maximum opening o_{eff} and sliding s_{eff}, consisting of both plastic and elastic components, are introduced. The cohesive zone behaves fully elasto-plasticity in Phase 2 before the effective plastic openings $o_{p,eff}$ or $s_{p,eff}$ reaches their corresponding plastic limit. Meanwhile, the damage index d_n and d_t in Phase 2 are set as zero:

$$o_{p,eff} \le o_{pl} \rightarrow d_n = 0 \tag{17}$$

$$s_{p,eff} \le s_{pl} \rightarrow d_t = 0 \tag{18}$$

which leads to an unloading with the initial stiffness (e.g. branch 1 - 1 in **Fig. 4 (a)** or **Fig. 4 (b)**).

The cohesive zone will subsequently perform combined damage and plasticity in Phase 3 after the effective plastic opening exceeds the plastic limit. The unloading traction in this phase declines to the plastic limit in a damage dominant manner (e.g. branch 2 - 2 in **Fig. 4 (a)**), in which the damage index is given as:

$$o_{p,eff} > o_{pl} \rightarrow d_n = 1 - \frac{o_{eff}\exp\left(-\frac{o_{eff}}{o_p}\right)}{o_{eff} - o_{pl}} \tag{19}$$

$$s_{p,eff} > s_{pl} \rightarrow d_t = 1 - \frac{s_{eff}\exp\left(-\frac{s_{eff}^2}{2s_p^2}\right)}{s_{eff} - s_{pl}} \tag{20}$$

Finally, the decohesion behavior with the combined damage and plasticity can be determined

through adjusting the plastic limit. The ratio of plastic energy dissipation in the total delamination work can be defined with a range from 0 to 1, by applying various plastic limit from 0 to infinity, leading to the delamination shifting from damage dominant unloading to plasticity dominant unloading.

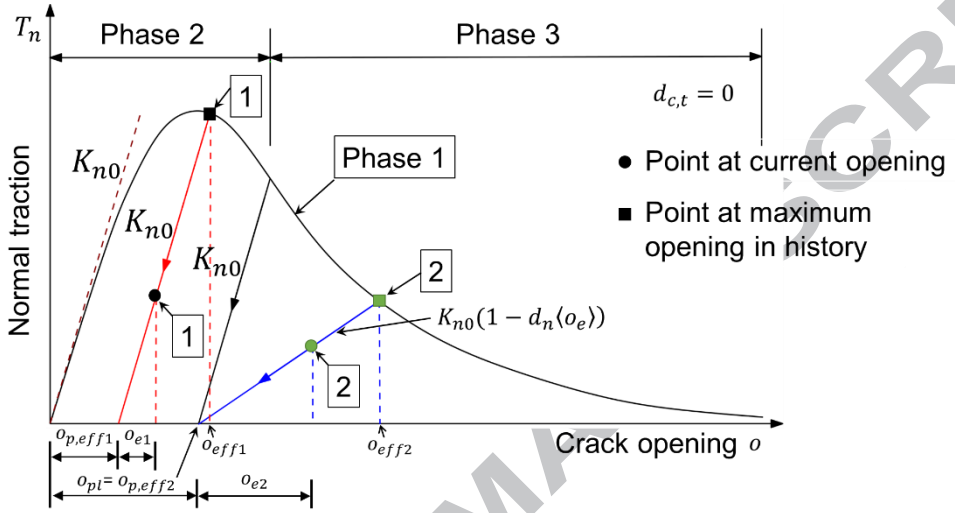

(a) Three phases of the combined damage-plasticity model in normal opening

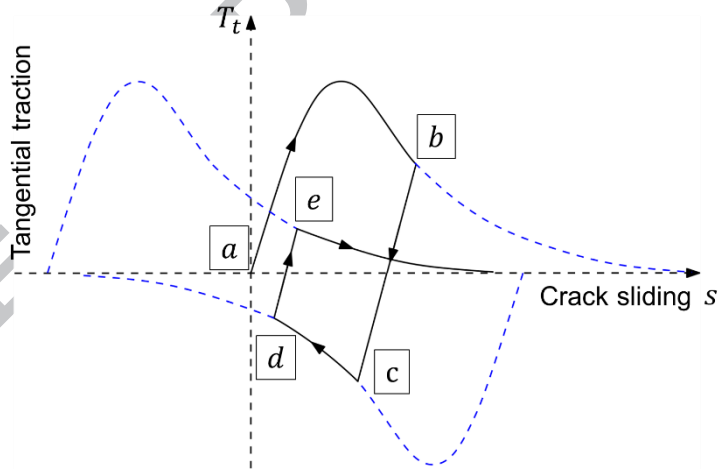

(b) Tangential behavior when reversing the loading direction at b and d during Phase 2

Fig. 4. The traction-separation law of the mixed-mode delamination model.

3 Numerical investigation on the impact breakage of laminated glass

3.1 Simulation conditions

In this section, a numerical model combining both the hyperelasticity of interlayer and the

mixed mode interfacial constitutive law is utilized to simulate the impact breakage of laminated glass. In order to investigate the breakage pattern and impact response of different glass make-ups of laminated glass, a glass beam comprising two glass panels subjected to hard body impact is performed. Commonly used glass types such as annealed glass (ANG), heat strengthened glass (HSG) and fully tempered glass (FTG) are selected for multiple combinations of glass make-ups.

3.1.1 Cracking model of glass material

Glass is commonly considered as a homogeneous isotropic material with ideal linear elastic behaviour until breakage [35], the dominant fracture is indicated to be caused by Mode I loading. The discrete crack model (DCM) based on the typical stress-displacement curve (**Fig. 5 (a)**) is used to model the Mode I cracking of glass in this study. The area under the stress-displacement curve represents the critical fracture energy in Mode I, G_{IC}. The crack initiation criterion based on the maximum principle stress is employed here. No separation occurs before the bond stress T_n reaches the tensile strength, f_t, and the separation $o = o_p = 0$ coincides with T_n being equal to f_t. The bond stress decreases when $o > o_p$ and finally drops to zero when $o = o_c$. The bond stress in the strain softening interval ($o_c > o > o_p$) is given by:

$$T_n = zf_t \tag{21}$$

z is the softening function and is defined with the following empirical formula:

$$z = \left[1 - \frac{a+b-1}{a+b}\exp\left(d(a + \frac{cb}{(a+b)(1-a-b)})\right)\right][a(1-d) + b(1-d)^c] \tag{22}$$

where a, b and c are the constants obtained by the curve fitting approach based on the experimental stress-displacement curve of material tests. a = 1.2, b = -1.0 and c =1.0 are adopted (**Fig. 5 (b)**) in the simulation based on the parametric study conducted by Chen [20]. d is the damage index given by:

$$d = \begin{cases} 0, & \text{if } o \le o_p \\ 1, & \text{if } o > o_c \\ \frac{o-o_p}{o_c-o_p}, & \text{otherwise} \end{cases} \tag{23}$$

The shear behaviour model is calculated using the penalty function method, and softening function z. The shear stress T_t of adjacent elements is calculated as follows:

$$T_t = 2\frac{s}{s_p}f_t z \tag{24}$$

where s is the sliding displacement, $s_p = 2hf_t/p_0$, h is the size of a particular element and p_0 is the penalty term. Sliding occurs when shear stress exceeding the shear strength and complete detachment occurs when the critical sliding s_p is met.

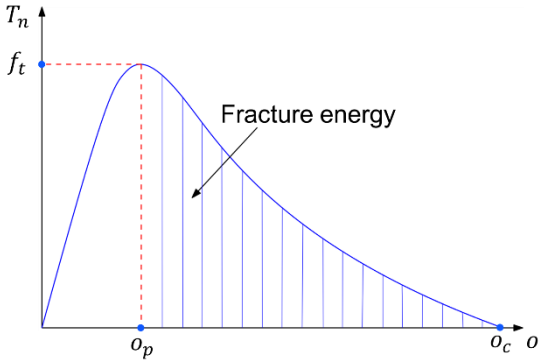

(a) Typical traction-separation law of DCM in normal direction

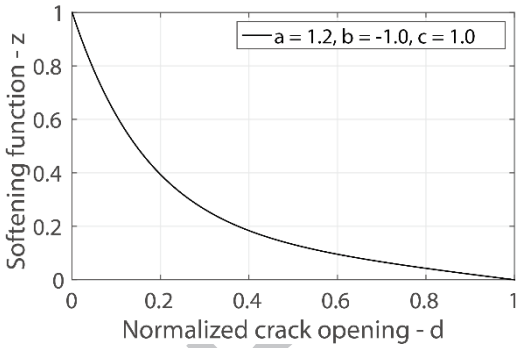

(b) Normalized bonding stress $z = T_n/f_t$ as function of normalized crack opening $d = (o\text{-}o_p)/(o_c\text{-}o_p)$

Fig. 5. Discrete crack model used in the FEM/DEM simulation.

The validity of discrete crack model of silica glass for simulating the typical crack pattern has been confirmed [36]. It is found that DCM is capable of capturing the crack initiation and propagation, and tracking the generation of many fragments along the glass thickness direction. The applicability of DCM in modelling thermally strengthened glass will be further investigated in the following sections.

3.1.2 Geometric and material property

The laminated glass beam of 1m long with both ends clamped by rubber cushion and steel channels is modelled with FEM/DEM using triangle plane stress elements. The LG specimen consists of two glass layers of 8 mm thick each and one 1.52 mm thick PVB interlayer. A fine mesh is applied to the section beneath the impactor after a convergence study, while coarse mesh is defined to the remaining area to reduce the consumption of computation time as shown in **Fig. 6**. The initial velocity of the hard impactor, which is a steel rectangle with a 40 mm radius semi-circular head, is set as 5 $\mathrm{m \cdot s^{-1}}$. The adapted Mooney-Rivlin model is utilized for the PVB with its failure stress defined as 25MPa and neglecting its rate-dependent characteristic. Both the

rubber cushion and impactor are assumed to be linear elastic material. The material properties of glass, PVB interlayer, impactor and rubber cushion are given in **Table 1**.

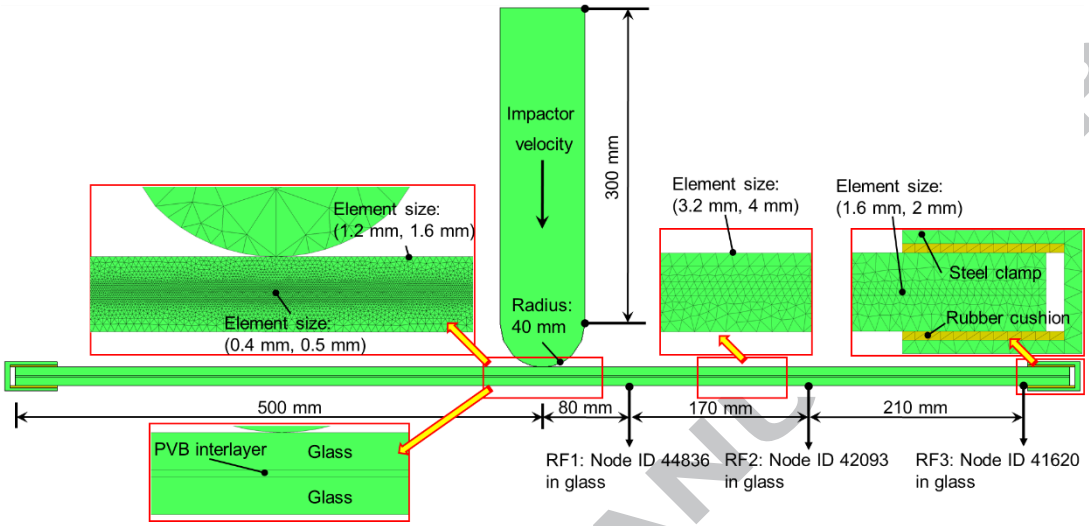

Fig. 6. Configuration and the mesh views of the simulation with double-layers laminated glass.

The interfacial bond is represented by zero-thickness joint element pairs having developed combined damage-plasticity interfacial constitutive model. Based on Dimitri's work [34], the ultimate separation o_t, s_t are defined as follows:

$$o_t = 3\frac{G_{IC}}{f_t} \tag{25}$$

$$s_t = 3\frac{G_{IIC}}{f_s} \tag{26}$$

where o_t, s_t are the ultimate separation in normal and tangential direction, respectively.

The plastic limit is a critical parameter to indicate the unloading behavior between damage and plasticity. Kolluri [37] proposed an approach using crack opening displacement profiles, which can be obtained through digital image correlation, to extract the plastic limit. However, the existing researches concerning the unloading delamination behavior of laminated glass is still limited since most cases used test methods to determine its interfacial bond, such as compressive shear test (CST) [23], peel test [38] and through-cracked tension test (TCT) [22], and did not take the un-loading scenario in to account. We define the plastic limit as the median value between the characteristic length o_p, s_p and the ultimate separation o_t, s_t as

$$o_{pl} = \frac{o_p + o_t}{2} = \left(\frac{3}{2} + \frac{1}{2\exp(1)}\right)\frac{G_{IC}}{f_t} \tag{27}$$

$$s_{pl} = \frac{s_p + s_t}{2} = \left(\frac{3}{2} + \frac{1}{2\sqrt{1/2\exp(1)}}\right)\frac{G_{IIC}}{f_s} \quad (28)$$

The influence of the coupling parameters on the tractions [33] implies the real coupling behaviour can only be obtained when G_{IC} is equal to G_{IIC}. Without much experimental evidence, both Mode I and Mode II fracture energy of the interfacial bond in this work are taken as 450 $\mathrm{J \cdot m^{-2}}$ for the low bond level of PVB based on the work by Pelfrene [31]. The bond properties adopted in simulating the mixed mode delamination is given in **Table 2**.

Table 1 Material properties used in the FEM/DEM analysis

Material	Glass	PVB	Impactor	Rubber
Density ($\mathrm{kg \cdot m^{-3}}$)	2500	1100	7850	1000
Young's modulus (GPa)	70	-	200	0.0023
Poisson ratio	0.2	0.49	0.3	0.45
f_t (MPa)	45 (ANG) 70 (HSG) 150 (FTG)	25	-	-
G_{CI} ($\mathrm{J \cdot m^{-2}}$)	10	-	-	-

Table 2 Bond properties used in delamination simulation

f_t (MPa)	f_s (MPa)	G_{IC} ($\mathrm{J \cdot m^{-2}}$)	G_{IIC} ($\mathrm{J \cdot m^{-2}}$)	o_{pl} (mm)	s_{pl} (mm)
5	2	450	450	1.5	0.346

3.2 Impact failure of double layered laminated glass

Multiple glass make-ups are modelled to investigate the impact response such as impact force, stresses at the critical locations and crack pattern. The impact duration is taken as 5 ms. The results of FEM/DEM simulation are compared with those obtained from experiment. These combinations are named with an order that the glass type located in the impact-side will be placed in the left side, e.g., ANG-FTG represents the specimen comprising annealed glass and fully tempered glass, where the annealed glass side will be subjected to the impact.

The time step of FEM/DEM computation should follow the principle that the time increment

cannot be greater than $h\sqrt{\rho/E}$, where h denotes the element size. The time step is then set as 5×10^{-10}s. In addition, the critical value of viscous damping k_s is estimated to be $2h\sqrt{E\rho}$ as suggested in Ref [27]. Because of the lacking parallel computation, the computational efficiency of FEM/DEM simulation is currently rather low. The computation of each impact case costs nearly one week using one CPU processor.

3.2.1 Experimental set up

The experiment is conducted using full sized LG panels (**Fig. 7**), of which the size is 1m × 1m with the same support condition as the numerical model. Each glass make-up in the experiment contains three repeated specimens. A high-speed camera is used to record the impact process of the specimens via a mirror underneath the laminated glass panel. Cracks are highlighted by two spotlights. Three accelerometers are glued to the inner surface (bottom surface) of glass panel identified as RF1, RF2 and RF3 respectively. These accelerometers are in the same location as the corresponding reference nodes in **Fig. 6**.

It is noted that the experimental results are based on the 3D set-up while the numerical modelling is carried out in 2-D manner. Their comparability is due to the radial symmetric nature at the initial cracking of such specimens and the 2-D plane model represents a typical section at the impact point.

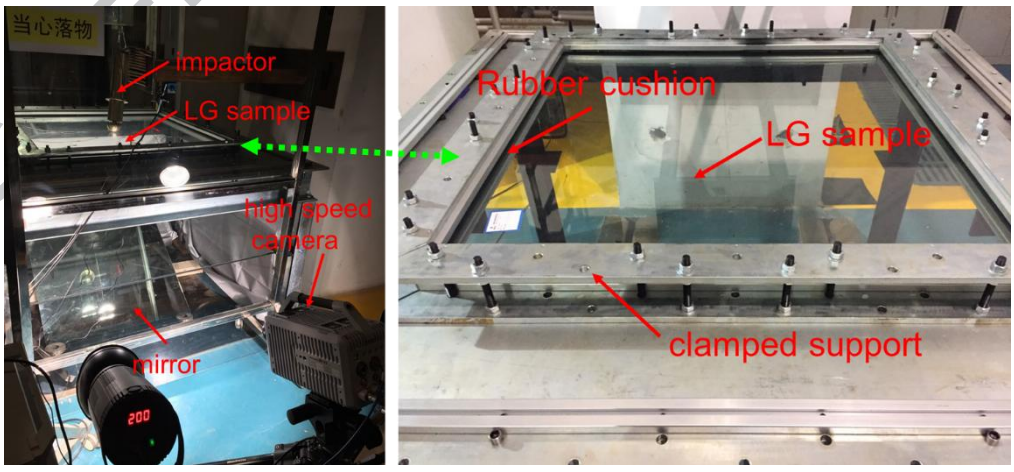

Fig. 7. The schematic illustration of the drop-weight experiment set-up.

3.2.2 Stresses wave propagation of glass

As shown in **Fig. 8**, the compressive wave generated by the impact will propagate from the loaded side to the free side in the thickness direction and subsequently reflects from the free surface of the bottom side in the form of tension stress waves, which consists of longitudinal (c_l), shear (c_s) and Rayleigh waves (c_r). The tension waves will further travel to the interfaces and upper surface in a dispersed manner and cause the vibration of reference nodes.

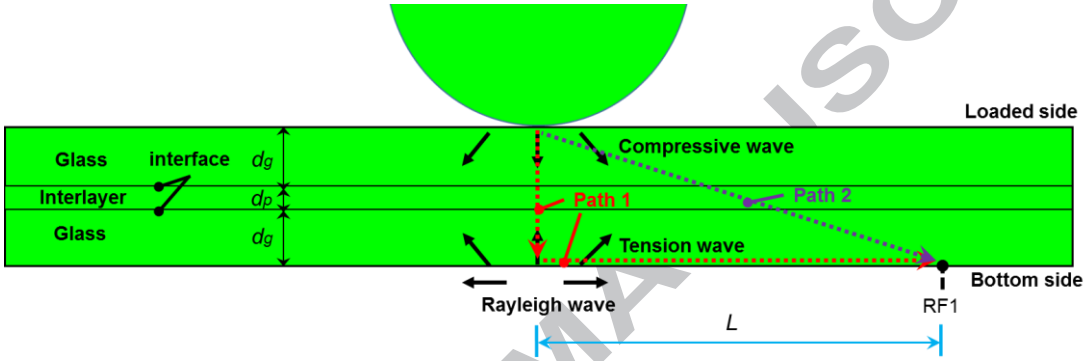

Fig. 8. The schematic diagram of stress wave propagation to RF1.

Firstly, the stress wave propagation in the laminated glass is investigated to determine the shortest travelling time of the stress waves hitting interface/boundary. **Fig. 9** shows the maximum principal stress vs. time in reference nodes RF1 to RF3 located at the bottom surface of glass. The stress wave propagation calculated by numerical results are compared with that of the experiment. The latter can be obtained through analyzing the lagging time between the initial responses of the corresponding accelerometers. A duration 0 - 0.3 ms is selected to identify the vibration of reference nodes.

In the numerical simulation of the specimens where the ANG or HSG side is subjected to impact (i.e., ANG-FTG in **Fig. 9 (a1)**, HSG-FTG in **Fig. 9 (b1)**, HSG-HSG in **Fig. 9 (c1)**), the stress wave travelling velocity V_p varies from 1680 to 2100 m/s. The velocity is negligibly higher in the specimens whose FTG side is subjected to the impact (i.e., FTG-ANG in **Fig. 9 (a2)**, FTG-HSG in **Fig. 9 (b2)**, FTG-FTG in **Fig. 9 (c2)**), varying from 1700 to 2125 m/s. From the theoretical prediction, the stress wave velocity in various glass types that have the same elastic modulus, is expected to be identical if the glass layer is perfectly bonded with the interlayer,

because the theoretical value of wave velocity is proportional to the square root of elastic modulus as shown in **Eq. (29)**:

$$\text{Longitudinal wave speed: } c_l = \sqrt{\frac{E(1-\mu)}{(1-2\mu)(1+\mu)\rho}}$$
$$\text{Shear wave speed: } c_s = \sqrt{\frac{E}{2(1+\mu)\rho}} \tag{29}$$
$$\text{Rayleigh wave speed: } c_r \approx 0.495 c_l$$

where E, μ and ρ represent the Young's modulus, poisson ratio and material density, respectively.

The difference of V_p in simulation are primarily due to the simultaneous occurrence of the local crushing and delamination. The local crushing crack occurs almost simultaneously when the impactor hits on the glass and leads to multiple wave reflection between glass fragments. Likewise, the interlaminar separation and delamination are also frequently observed, causing a great deal of wave reflection amongst layers as well. Both factors are responsible for the delaying in the stress wave propagation and leading to the various lagging time of the initial vibration of the reference nodes.

$$\begin{aligned} t_1 &\approx 2t_{glass,t} + t_{pvb} + 2t_{interface} + t_{glass,l} \\ &= 2\frac{d_g}{c_l}\Big|_{glass} + \frac{d_p}{c_l}\Big|_{pvb} + 2t_{interface} + \frac{L}{c_l}\Big|_{glass} \\ &\approx 0.021ms + 2t_{interface} \end{aligned} \tag{30}$$

where $t_{glass,t}$, t_{pvb}, $t_{interface}$ and $t_{glass,l}$ represent the time requested for stress wave travelling through glass thickness, PVB interlayer, interface and distance L, respectively. L is the distance from the center of bottom side to the node RF1. d_g, d_p are the thickness of glass layer and PVB interlayer, respectively. It is apparent that the longitudinal stress wave (glass: c_l = 5654 m/s, PVB: c_l = 321 m/s) will travel to RF1 with the shortest time, the initial vibration of RF1 is thus predicted to be caused by the longitudinal stress wave. The travelling time t_1 should be no less than 0.021 ms as shown in **Eq. (30)**, since the time spent for wave propagates across the interface, that is, $t_{interface}$, cannot be precisely estimated. Such theoretical propagation time (0.021 ms) is highly close to the value obtained in the numerical simulation (0.02 ms). It also reveals that the interface has little influence on reducing the wave velocity when wave propagating from loaded layer to the bottom layer at the beginning of impact.

Fig. 9 also shows the initial vibration time of RF3 near the support. It takes approximately 0.14 - 0.165 ms for the first stress wave reaching RF3 in the simulation, which means the symmetry of the stress wave propagation is only rigorously true in less than 0.165 ms after which, the reflected wave from the support will be mingled and the radial symmetry will be lost. Compared with the theoretical value of the initial vibration time (0.089 ms) using **Eq. (30)**, the stress wave is significantly delayed because of the wave reflections at interfaces. Such delaying is observed by other researchers as well [39].

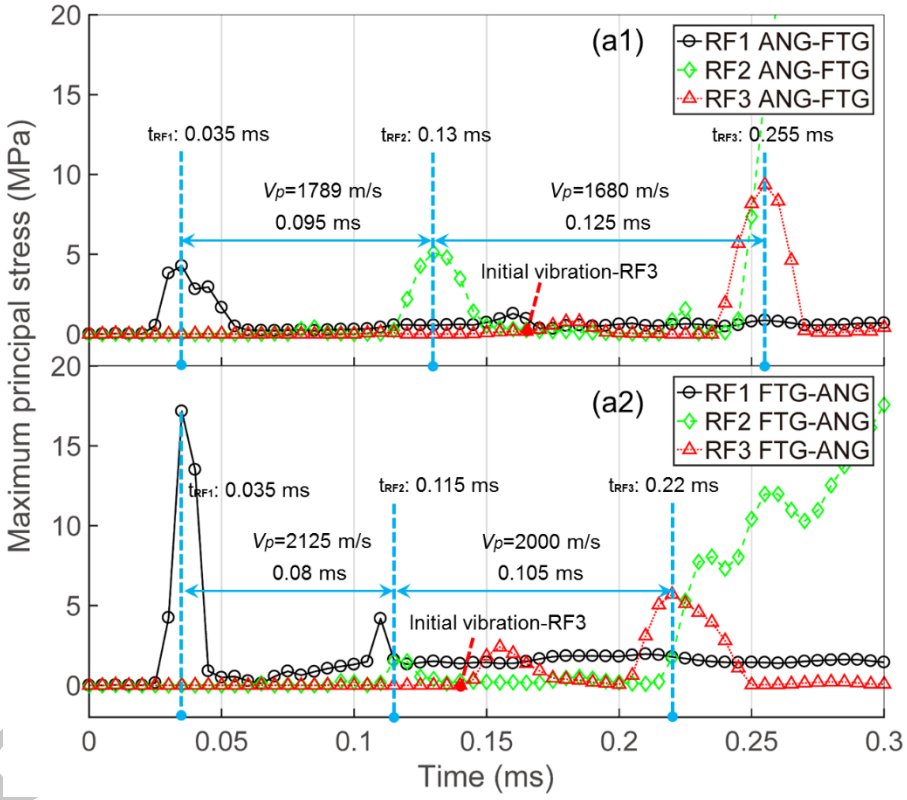

(a) Different glass types (ANG and FTG) adopted in two glass layers

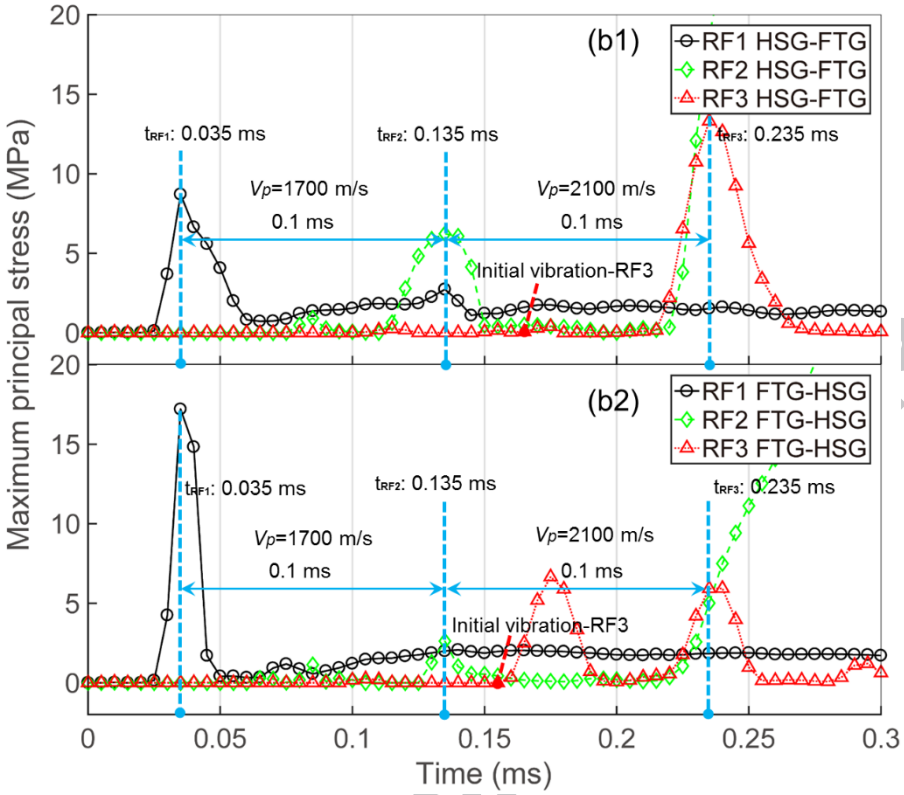

(b) Different glass types (HSG and FTG) adopted in two glass layers

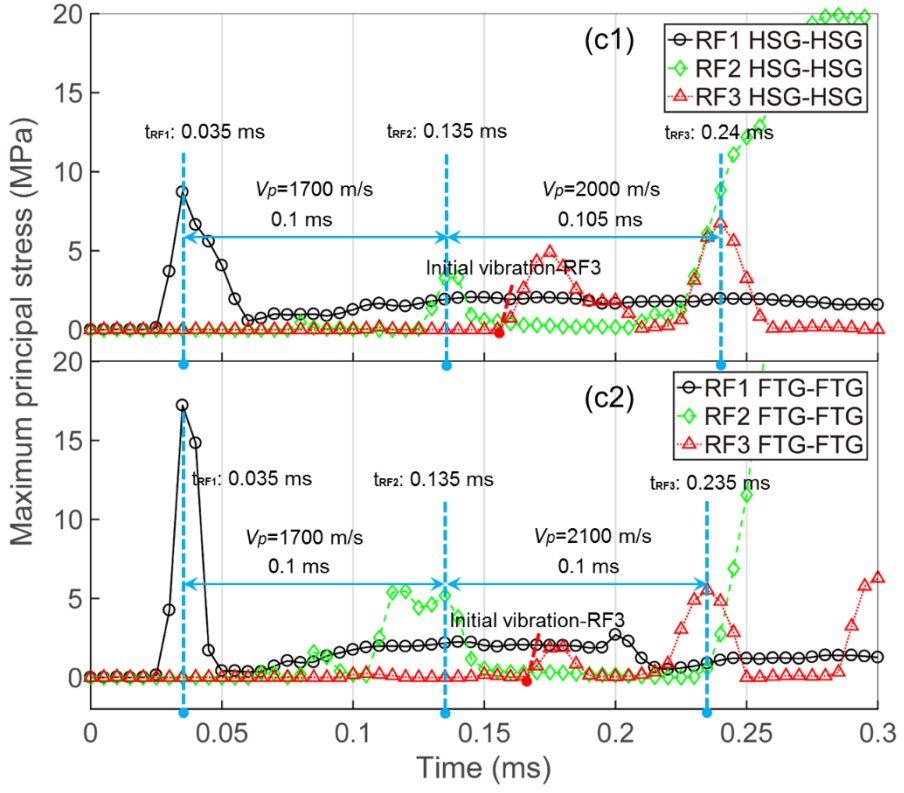

(c) Same glass type (HSG or FTG) adopted in two glass layers

Fig. 9. Maximum principal stress variation of reference nodes in FEM/DEM simulation.

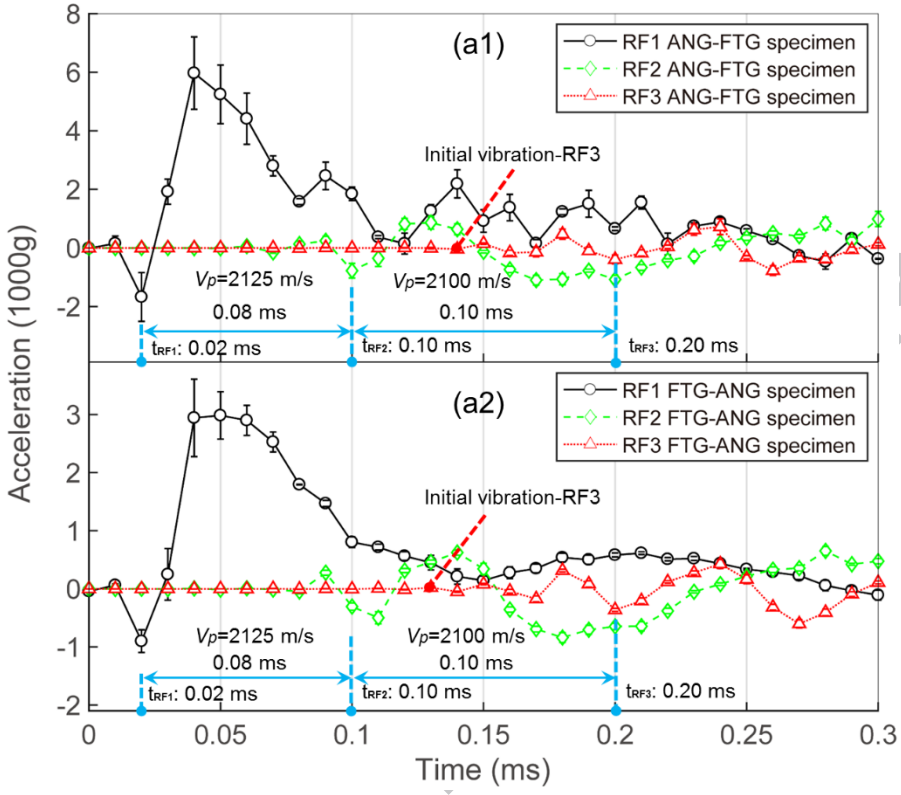

(a) Different glass types (ANG and FTG) adopted in two glass layers

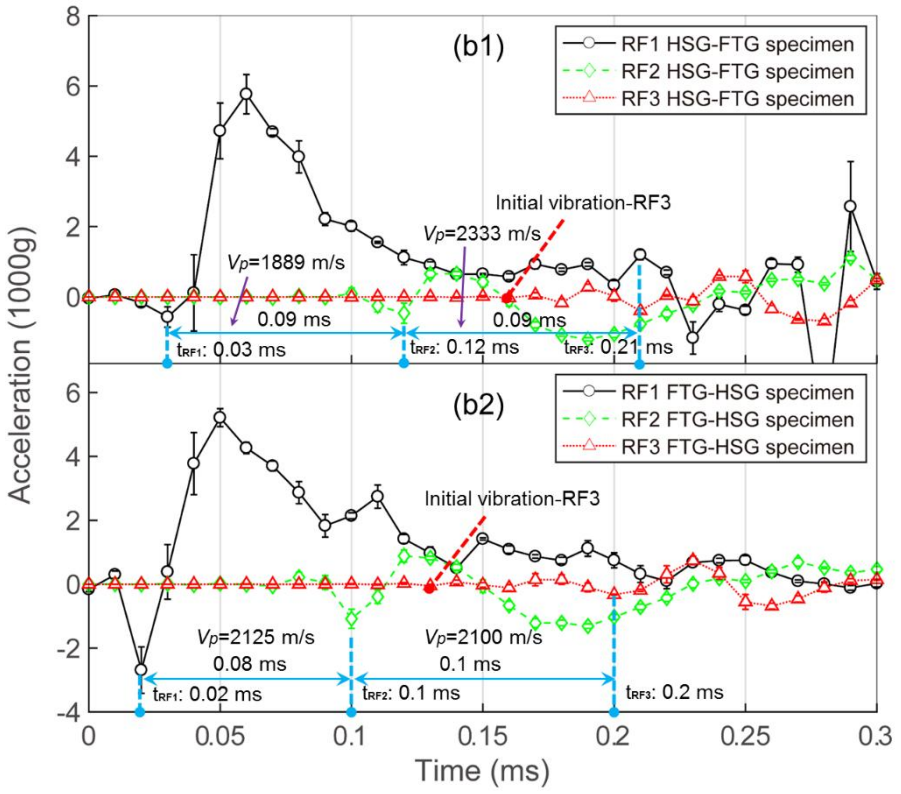

(b) Different glass types (HSG and FTG) adopted in two glass layers

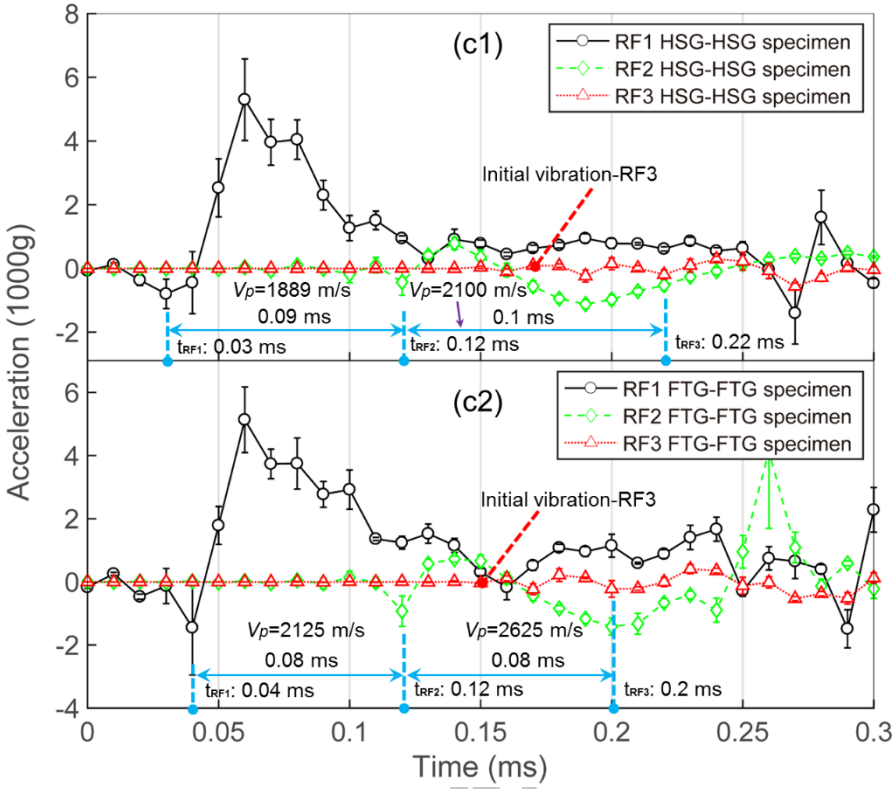

(c) Same glass type (HSG or FTG) adopted in two glass layers

Fig. 10. Acceleration history of reference nodes in the experiment.

Fig. 10 shows the mean acceleration history data of reference nodes with its corresponding standard deviation recorded in the experiment. It is worth noting that the data acquisition will not be triggered until the acceleration of the RF1 accelerometer exceeds the predefined value. Thus, the time consumed by the stress wave travelling from the impact point to RF1 cannot be obtained since the moment of impact is not exactly located.

In the specimens where ANG and HSG glass is the impact side (i.e., ANG-FTG in **Fig. 10 (a1)**, HSG-FTG in **Fig. 10 (b1)**, HSG-HSG in **Fig. 10 (c1)**), the lagging time between the trough of acceleration data curves shows the stress wave propagation speed varies from 1889 to 2333 m/s. It has a slight increase in the specimens where FTG receives impact (i.e., FTG-ANG in **Fig. 10 (a2)**, FTG-HSG in **Fig. 10 (b2)**, FTG-FTG in **Fig. 10 (c2)**), which ranges from 2100 to 2625 m/s.

The average stress wave propagation velocity from RF1 to RF2, and RF2 to RF3 in both FEM/DEM simulation and experiment is shown in **Fig. 11**. It can be seen that the stress wave travels faster in the experiment. The strengthening process of HSG and FTG produce the internal

residual stress in the thickness direction, creating a central tension zone within the glass section and a compressive zone around the glass surface. It is believed that the energy induced due to the prestress field will accelerate the travelling of the stress wave, which is evidenced by the incremental growth in propagation speed amongst ANG, HSG and FTG.

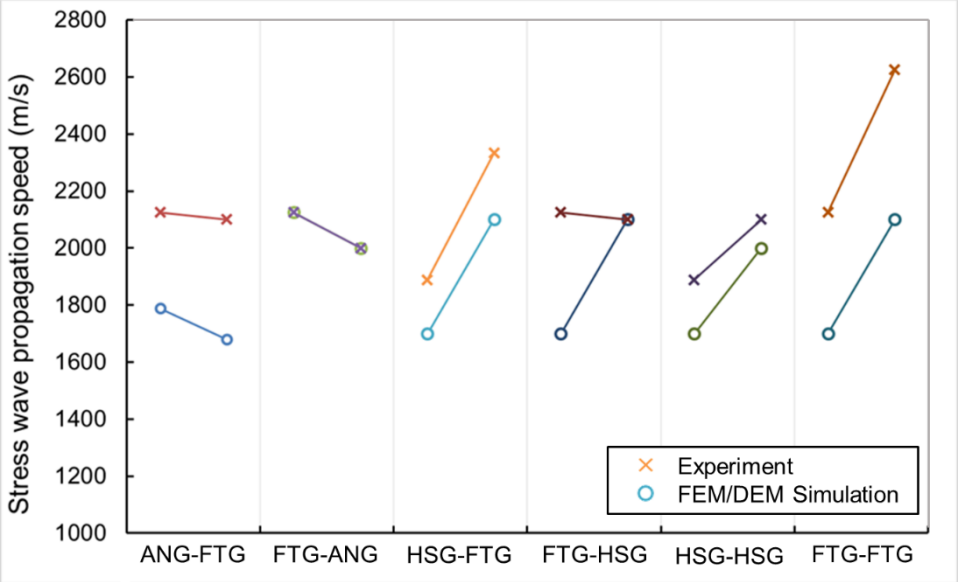

Fig. 11. Average stress wave propagation speed of FEM/DEM simulation and experiment.

3.2.3 Impact force

The normalized impact force is examined to investigate the general variation of the impact force during impact and the contact duration, which may be used to evaluate the likelihood of glass breakage. The assessment of normalized impact force in FEM/DEM simulation at 5 ms is performed by means of the experimental results as depicted in **Fig. 12**. Each glass make-up has three recorded force signals in the experiment. The impact forces are normalized to their largest value, respectively.

From the experimental results in **Fig. 12**, it can be seen that the experimental impact force presents an oscillatory phase at the beginning of contact that is composed of several cycles, instead of presenting only one peak before impact force drops to zero. This is mainly due to the interactive effect between impactor and glass panel. The time lag between the neighboring

oscillatory peak force is approximately 0.165 ms which is in accordance with that consumed by the stress wave propagating from the impact point to the support. The ending of the oscillatory phase where impact force has an evidently large drop, could be used to identify the first breakage of glass layer. According to the high consistency of the impact force in all FTG-ANG specimens (**Fig. 12 (a2)**), this group of specimens are selected to show the correlation of the oscillatory phase and the glass breakage. The initial oscillation phase of FTG-ANG specimens presents two peak values before its evident declining to nearly 10% - 20% of the maximum impact force. The first glass breakage of glass layer, which is the ANG layer in all three specimens, occurs at the end of the oscillatory phase and is denoted by the red circle in **Fig. 12 (a2)**. It is followed by a minor increase to nearly 40% peak force and a drop to zero at 2.39 ms, which indicates the second breakage of FTG layer.

However, in the numerical simulation, especially the specimens having ANG and HSG at the loaded side (i.e., ANG-FTG in **Fig. 12 (a1)**, HSG-FTG in **Fig. 12 (b1)**, HSG-HSG in **Fig. 12 (c1)**), do not exhibit the initial oscillatory phase. The absence of this phase is attributed to the immediate occurrence of the crushing cracks in the loaded side when the impactor strikes the glass. The impact force started a rapid declining when the crushing cracks appear, and a full oscillatory phase is thus not obtained. In the FEM/DEM simulation, after cracks penetrate through the top glass thickness (in less than 0.025 ms), the glass fragments stay in place and experience compression. Such compressive behavior is not stable because fragments will easily come loose and splash around. Because of the existence of the functioning glass fragments, the impact force increases to nearly 40% peak and may become unstable shortly. Such features after first glass breakage agree well with the experimental observation.

In simulating the specimens whose FTG layer is subjected to the impact (i.e., FTG-ANG in **Fig. 12 (a2)**, FTG-HSG in **Fig. 12 (b2)**, FTG-FTG in **Fig. 12 (c2)**), because FTG has higher tensile strength, crushing cracks does not appear immediately. An initial oscillation phase with a full peak of impact force at 0.25 ms can then be observed. This full peak shows high consistency with the experimental results.

Several specimens in the experiment, e.g., the first HSG-FTG specimen that is denoted by dashed line (**Fig. 12 (b1)**), breaks first in the bottom glass layer. This cracking sequence cannot

be produced in the FEM/DEM simulation, of which the glass breakage always initiate with the crushing cracks in the top layer.

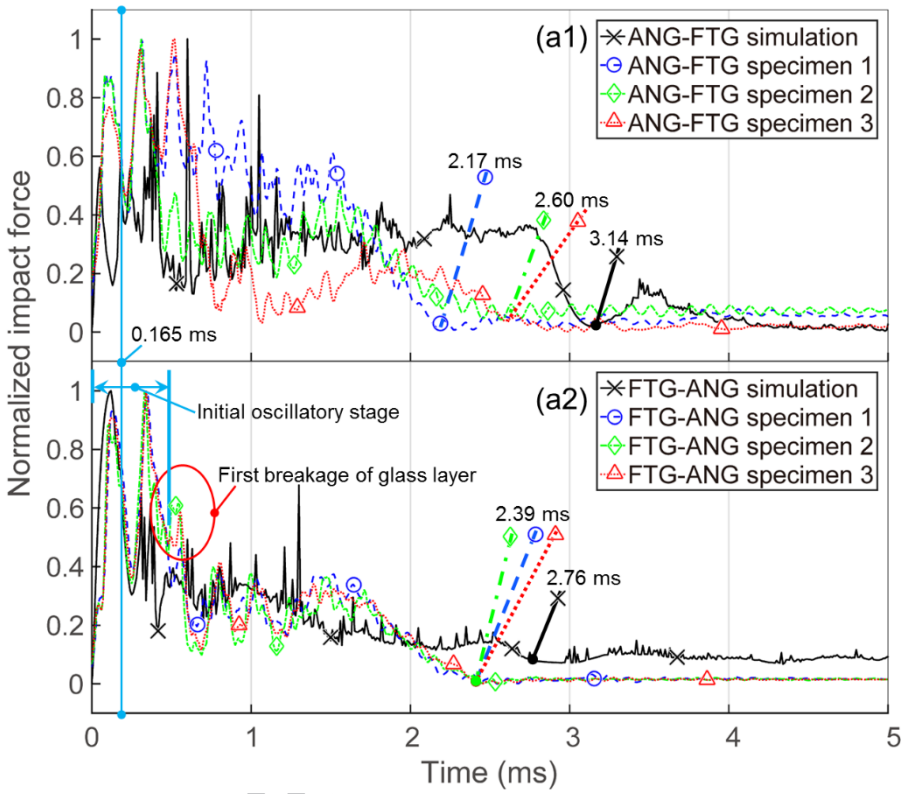

(a) Different glass types (ANG and FTG) adopted in two glass layers

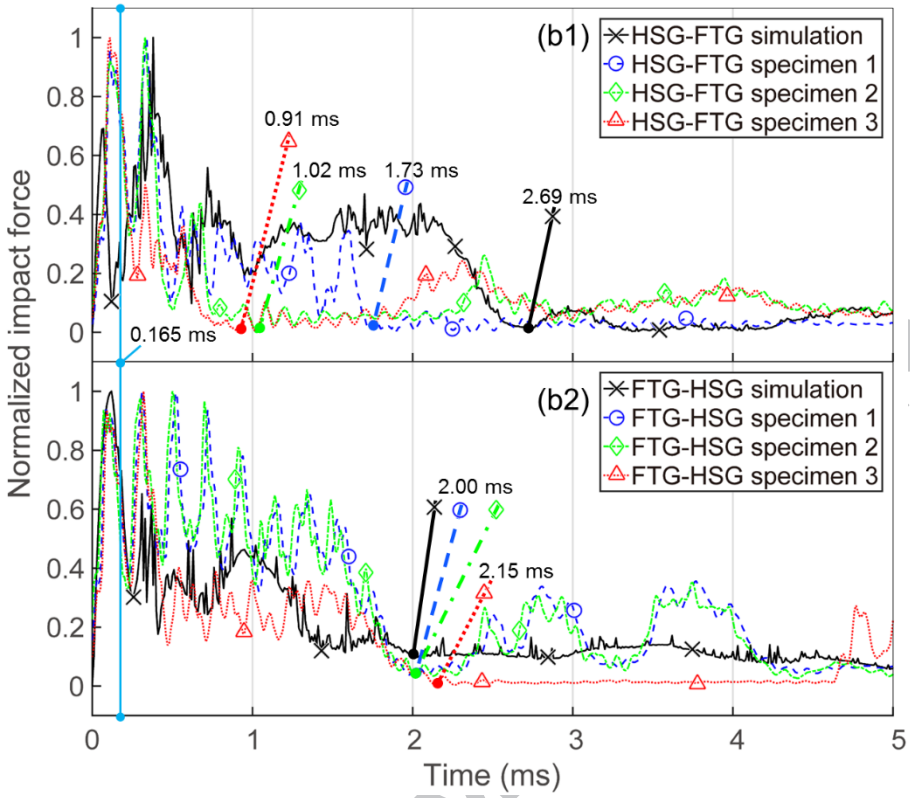

(b) Different glass types (HSG and FTG) adopted in two glass layers

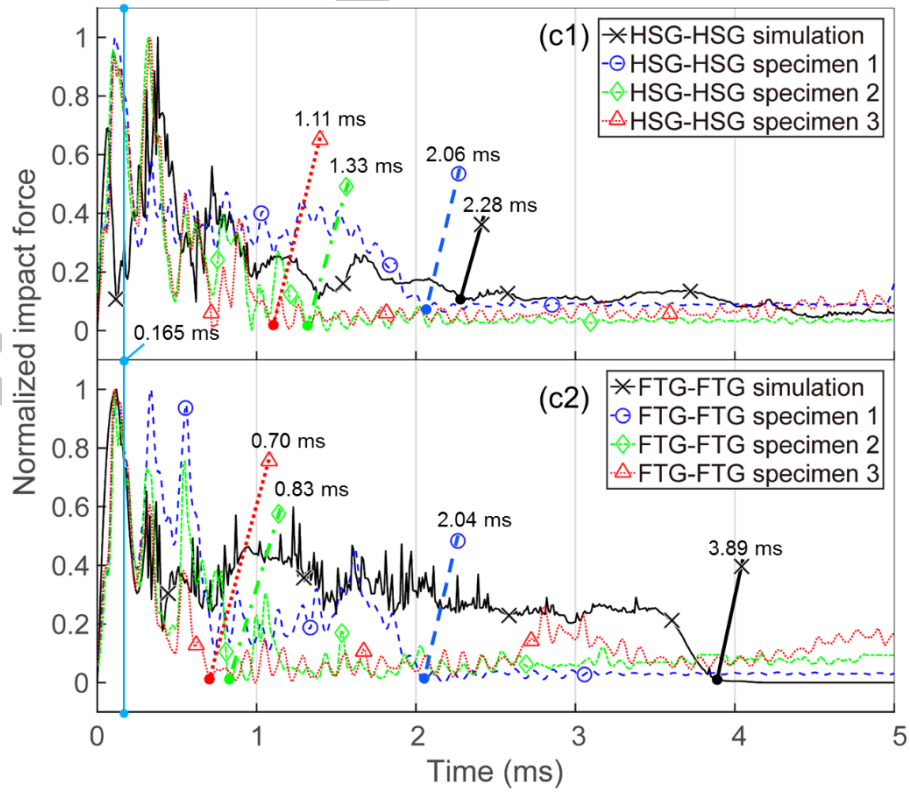

(c) Same glass type (HSG or FTG) adopted in two glass layers

Fig. 12. Normalized impact force history of FEM/DEM simulation and experiment.

The contact duration was examined before both glass layers fail, i.e., impact force drops to zero permanently. It can be seen in **Fig. 12** that the FEM/DEM simulation overestimates the contact duration compared with the experiment results. Only the contact duration of FTG-HSG specimen is close to the experimental one. The longer contact duration in FEM/DEM simulation is mainly because that the numerical results for the duration of residual impact resistance after first glass breakage is longer. This reason is that the cracks always initiate in the impact side in numerical simulation.

From the specimens containing FTG layer subjected to impact (i.e., FTG-ANG in **Fig. 12 (a2)**, FTG-HSG in **Fig. 12 (b2)**, FTG-FTG in **Fig. 12 (c2)**), the impact force in FEM/DEM simulation always exhibits a plateau that is nearly 40% of the peak impact force after the first glass breakage. Such plateau leads to larger contact duration that is more than 2.69 ms. Similar plateau can be found in a few experimental results as well, such as the 2nd ANG-FTG (**Fig. 12 (a1)**), the 1st HSG-FTG (**Fig. 12 (b1)**) and the 1st FTG-FTG (**Fig. 12 (c2)**) specimens. However, such plateau cannot be observed in other experimental results with the same glass make-up, because the opposite cracking sequence of glass layers leads to the earlier breakage of both glass layers.

It can be concluded that the experimental results without the plateau in the impact force vs. time curve imply that breakage occurs first in the bottom glass layer. This conclusion can be supported by analyzing the high speed photos. The high speed photos of 1st and 2nd FTG-FTG specimens are presented as example in **Fig. 13**. The cracking fronts are located in each frame having an interval of 0.08 ms. The time of the crack initiation is found to be 0.08 ms after the high speed camera was triggered. It is notable that the time points that these high speed photos are recorded are different from force and acceleration signals, because high speed camera and data acquisition system have different triggering mechanisms.

Fig. 13 shows that these two FTG-FTG specimens are in different cracking sequences. In the 2nd FTG-FTG specimen, the radial cracks in the bottom glass layer are firstly observed (**Fig. 13 (b)**). It is followed by the rippled cracks generated in the loaded layer. In this cracking sequence, the impact force of the 2nd FTG-FTG specimen as shown in **Fig. 12 (c2)** does not

present a plateau and drops to zero at 0.83 ms.

On the contrary, the rippled cracks firstly initiate in the loaded layer in the 1st FTG-FTG specimen (**Fig. 13 (a)**), the radial cracks appear in the bottom layer afterwards. In this case, the impact force response curve has a plateau at nearly 50% peak force and drops to zero at 2.04 ms.

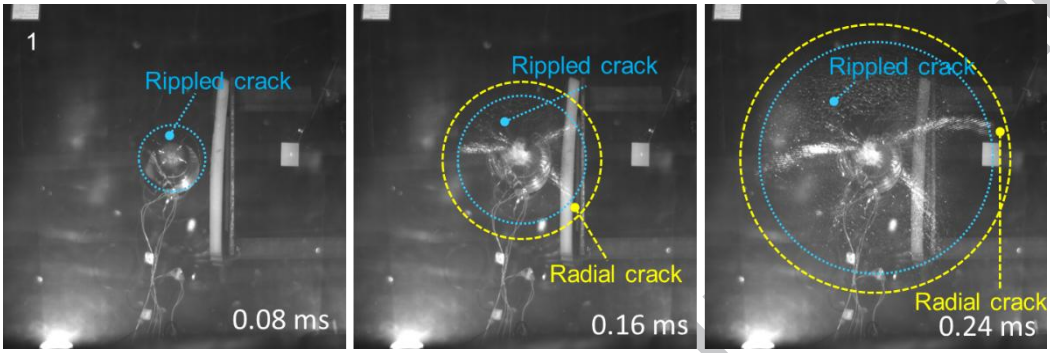

(a) 1st specimen with rippled cracks generated first in the loaded layer

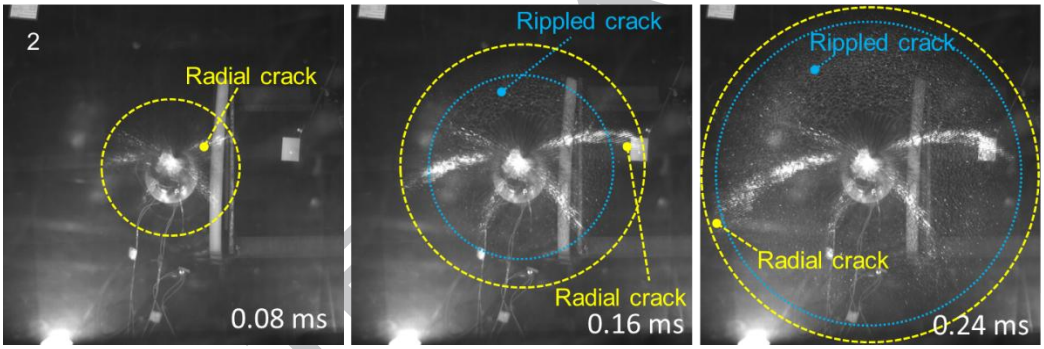

(b) 2nd specimen with radial cracks generated first in the bottom layer

Fig. 13. Cracking sequence of selected FTG-FTG specimens.

3.2.4 Crack pattern and delamination

Crack pattern and delamination behavior is further investigated to identify their correlation and the applicability of the mixed mode delamination model proposed in this article. **Fig. 14** shows the key region of the FEM/DEM simulation at 5 ms. The scale factors of the deformation of various LG configurations have been adjusted to manifest the characteristics of cracks and delamination.

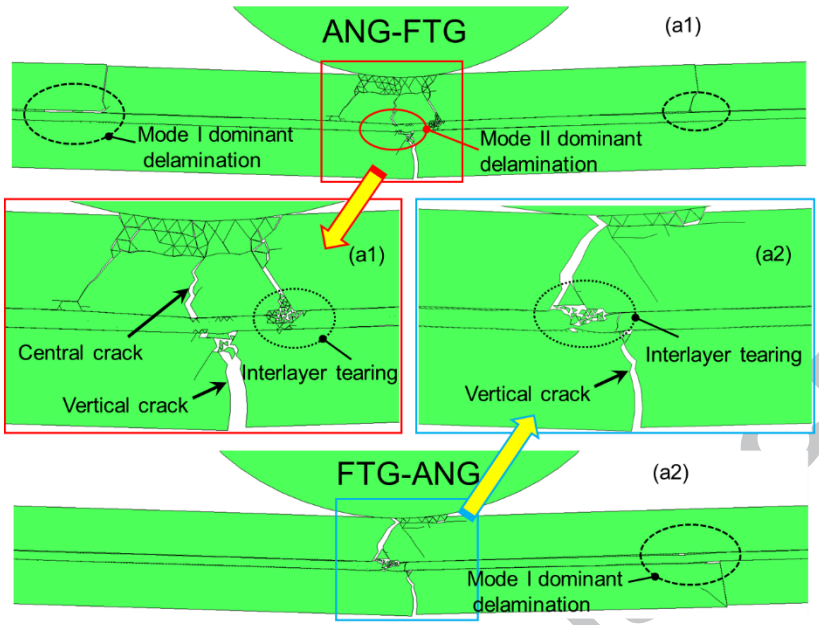

(a) Different glass types (ANG and FTG) adopted in two glass layers

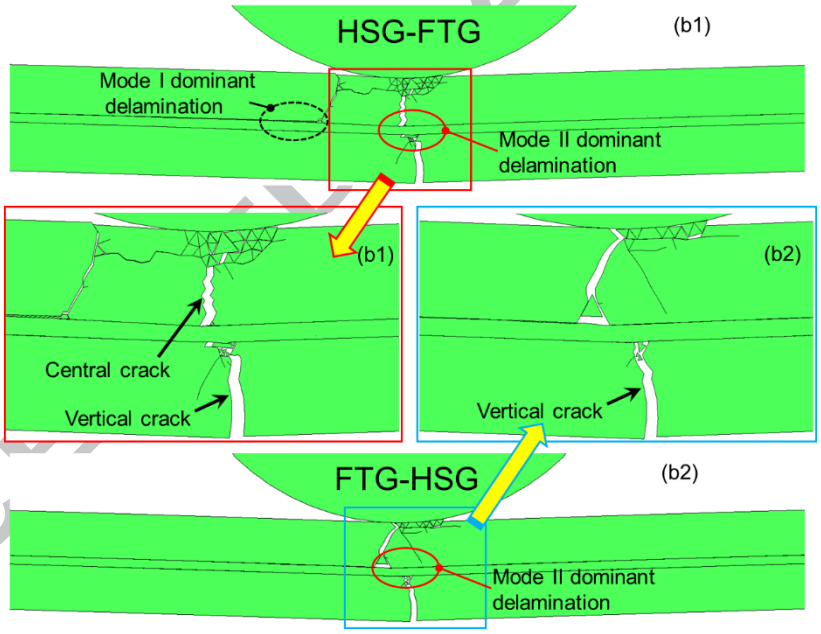

(b) Different glass types (HSG and FTG) adopted in two glass layers

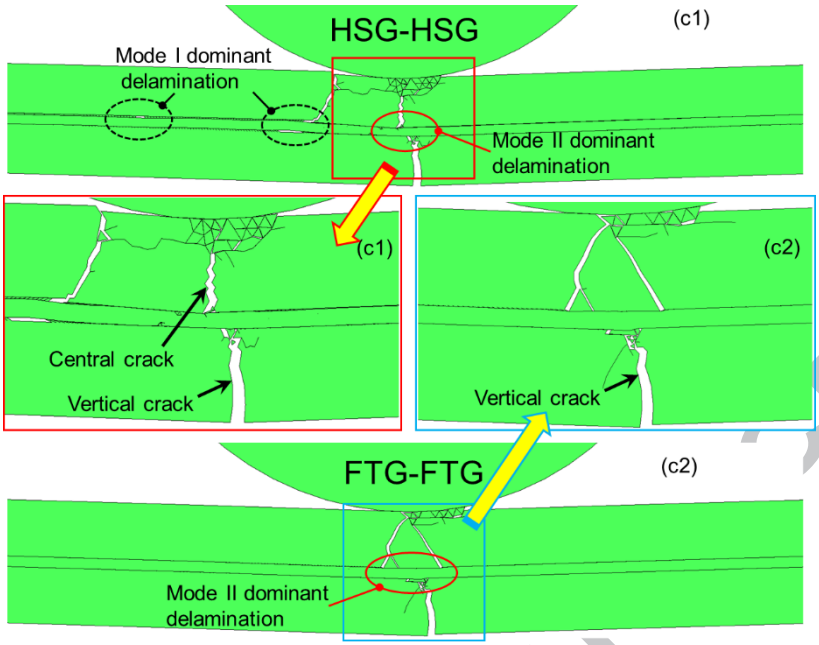

(c) Same glass type (HSG or FTG) adopted in two glass layers

Fig. 14. Crack patterns and delamination observations of FEM/DEM simulation.

From the crack pattern of the loaded layer, the ANG layer (**Fig. 14 (a1)**) exhibits a cone crack whose feature length D_1 and D_2 (see **Fig. 15 (a)**) are approximately 10.5 mm and 16 mm, respectively. The cone crack is induced from the crushing cracks that concentrated in the zone of the feature length D_1. However, the HSG layer (**Fig. 14 (b1, c1)**) only shows half cone crack. Most crushing cracks concentrate in the opposite half zone (i.e., the right side from the impact point), which does not produce the cone crack. It is worth noting that the width of the central crack in the HSG layer is much larger than that of the ANG layer, and has the trend of extending to the left. The crushing cracks in the right side result in the horizontal motion of impactor that tends to move left. Such trend will apply large horizontal force on the left un-cracked zone, further broadens the central crack and promotes Mode II dominant delamination. The crack pattern in the ANG layer shows a similar process that the horizontal motion of impactor, which is resulted from the crushing cracks in the left, drives the propagation of cone crack in the right un-cracked zone. Such motion causes large local strain between cone crack tip and interlayer, further leads to the interlayer tearing. In the specimens where either HSG or ANG layer is subjected to impact, Mode II dominant delamination can be identified between the cone cracked zone and interlayer. In the

case where the FTG layer receives impact (**Fig. 14 (a2, b2, c2)**), a triangle crack comprising two oblique cracks is captured instead of the cone crack. However, similar horizontal motion that is caused by the crushing crack in the right side (**Fig. 14 (a2)**) can be found as well. It finally leads to the interlayer tearing in the FTG-ANG specimen.

From the crack pattern of the bottom layer, only vertical crack originated from the outmost surface of the bottom layer is produced in all specimens. The tension stress waves, which is generated from the reflection of the compressive waves from the bottom surface, trigger the initiation of vertical crack near the center of the bottom surface. The vertical crack propagates to the interlayer with a trend of approaching the nearest crack tip in the impacted layer. The growth of vertical crack finally leads to partial delamination, which is similar to the experimental observation that has been reported in Jan's work [40] (**Fig. 15 (b)**).

(a) Herztian cone crack [41]

(b) Partial delamination in the bending test of LG beam [40]

(c) Partial delamination in the impact test

Fig. 15. Experimental observation of cone crack and delamination.

From the delamination behavior in the simulation, two types of delamination can be classified based on the ratio of the work-of-separation to work-of-sliding at the bond failure of interface. This ratio is used to determine the dominant status and can be calculated as follows:

$$\varphi = \frac{\max\{G_I\}}{\max\{G_{II}\}} = \frac{\max\left\{\int_0^{o_1} T_n(o,s)|_{s=0}\,do\right\}}{\max\left\{\int_0^{s_1} T_t(o,s)|_{o=0}\,ds\right\}} \tag{31}$$

where max{·} denotes the maximum value of the work-of-separation at the breaking point of the joint interface elements; o_1 and s_1 represent the opening and sliding at the maximum work-of-separation, respectively. The ratio φ will be calculated using **Eq. (31)** at the break of the reference joint elements. If $\varphi > 1$, the delamination is deemed as the Mode I dominant status; otherwise, is Mode II dominant.

As shown in **Fig. 14**, the partial delamination in conjunction with the vertical crack in the bottom layer is observed. The partial delamination is mainly resulted from the relative sliding of the interlayer and the bottom glass layer, that is, being dominated by Mode II behavior. Similar partial delamination can be found in the static bending test of LG beam (**Fig. 15 (b)**) and the impact tests of LG panel (**Fig. 15 (c)**) as well. In the impact test, the radial cracks in the bottom layer result in glass fragments that are in shape of beams. The glass beams present evident vertical crack and Mode II dominant delamination underneath the impact point.

Conversely, the delamination dominated by Mode I behavior usually occurs in the vicinity of the cone crack tips and vertical cracks in the loaded layer. Mode I delamination is denoted by dashed circles in **Fig. 14**. Both cone crack and vertical cracks in the loaded layer cut off the top glass layer and isolate the neighboring parts of glass. The glass parts in both sides are clamped, thus, become a cantilever beam with the bottom surface glued by the interlayer. Whereas the central glass parts, i.e., cone cracked glass fragments, will continue moving downward under impact. This consequently amplify the difference in vertical motion between the central glass parts and the glass parts in both sides. The interlayer then has the trend to be peeled off from the glass parts in both sides, leading to Mode I dominant load in the interface.

In the experimental case where the ANG layer sustains impact, the high speed photos are shown in **Fig. 16** to illustrate the growth of crack pattern and delamination. At the beginning of impact, a cone crack can be observed in the loaded glass layer. The delamination under the impact point then continue to extend until covering a zone with diameter of approximately 120 mm before the bottom layer breaks. The experimental results present a similar delamination growth process to the FEM/DEM simulation, showing a Mode I dominant delamination zone beneath the impact and a further Mode II dominant delamination zone.

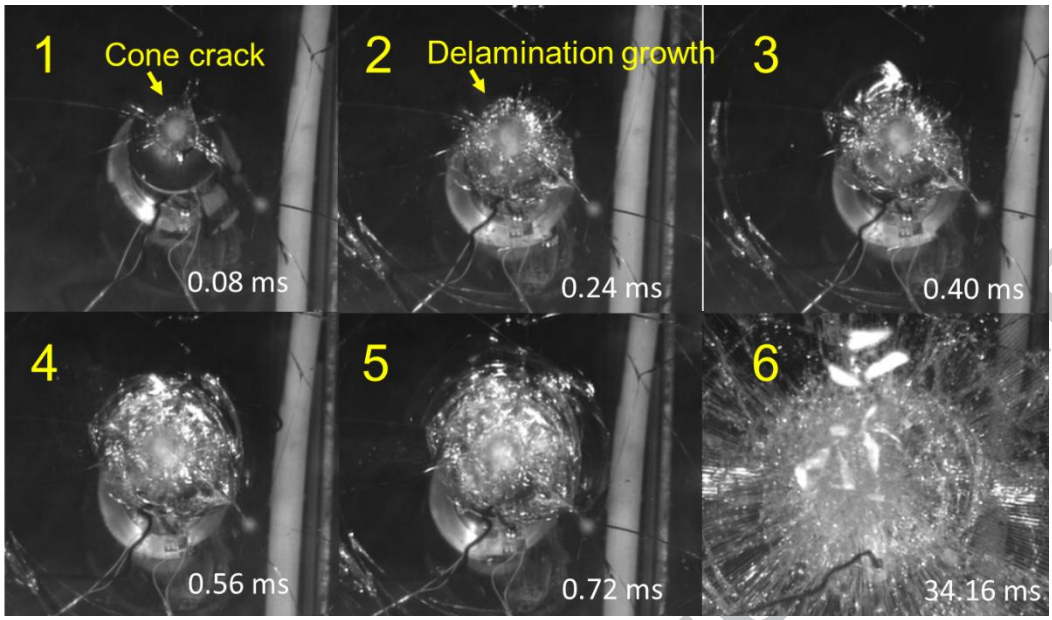

Fig. 16. Crack pattern and delamination growth of ANG-FTG specimen.

In the experimental case where the strengthened glass (HSG, FTG) sustains impact, a FTG-FTG specimen is taken as example to present the delamination between the loaded layer and PVB interlayer. In **Fig. 17 (a)**, the crushing cracks concentrate on a disk zone of 30 mm diameter at the impact point. Similar to the delamination observation of FTG-FTG specimen in FEM/DEM simulation (**Fig. 14**), delamination growth is not evident at the interface between the loaded layer and interlayer with only a small Mode II dominant delamination zone beneath the crushing cracks can be seen. **Fig. 17 (b)** shows that partial delamination with a vertical crack at the center of glass panel. Such results reveal that both typical delamination behavior near the impact point in the experiment can be produced in the FEM/DEM simulation. However, the process that the fully tempered glass fractures into dices cannot be modelled. It may lead to large discrepancy when analyzing the impact response in the following process of impact.

Overall, when compared with the experimental observation, the shortcoming of the discrete crack model in modelling the internal residual stress of fully tempered glass leads to the unavailability in presenting realistic crack patterns and glass fragmentation. However, this model is considered to be able to model the typical crack pattern near the impact point. As the major concern of this article, the validation of the typical delamination behavior shows high consistency with the experimental observation, showing that the combined damage–plasticity model

implemented in FEM/DEM performs efficiently in the mixed mode loading condition.

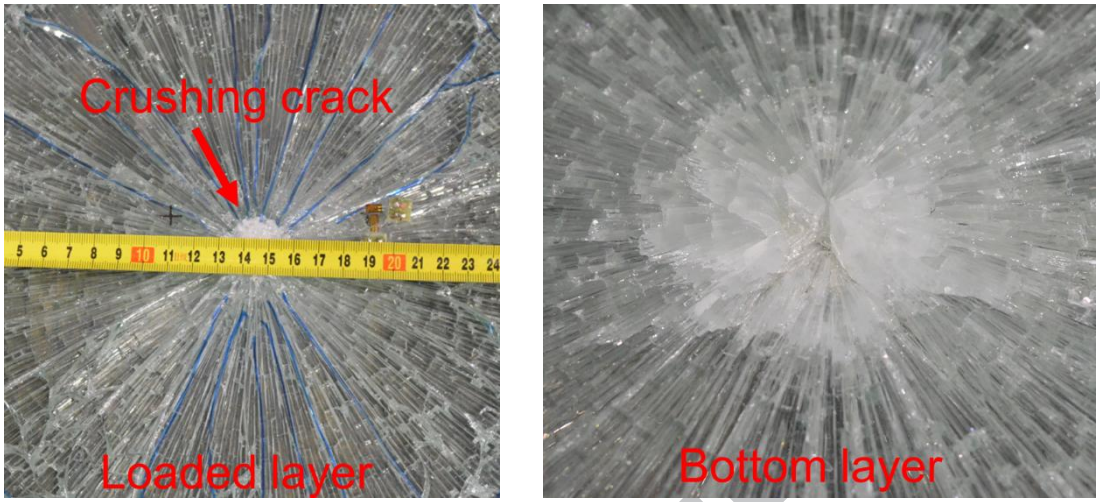

(a) Crack pattern in the loaded layer (b) Crack pattern in the bottom layer

Fig. 17. Experimental observations of delamination in FTG-FTG specimen.

4 Conclusions

The paper presents a numerical modelling approach encompassing the discrete crack model for glass, the hyperelastic model for PVB interlayers and the mixed mode interfacial constitutive model for glass/PVB interfaces to simulate the impact breakage of the laminated glass by using FEM/DEM. The comparison between experimental results and numerical simulation is carried out to confirm the validity of modelling.

The stress wave propagation in the numerical simulation agrees well with the experimental investigation as well as the analytical result. It can be deduced that both the crushing crack coinciding with the impact and delamination will result in the significant decrease in the stress wave travelling.

The lagging time of the stress wave propagating to the supporting boundary is obtained. In the lagging time, the specimens, where the FTG layer sustains impact, can reproduce the variation of the impact force satisfactorily, and reveal the peak in impact force. Whereas the specimens of which either ANG or HSG acts as the loaded layer, cannot capture the oscillatory phase in the impact force vs. time curves at the beginning of impact. Most of the numerical results

overestimate the contact duration. While the peak force after first glass breakage in FEM/DEM simulation is approximately 40% of the peak value prior to the second glass breakage, which agrees well with the experimental results.

The drawback of the discrete crack model in modelling the strengthened glass (HSG and FTG) is identified in this study. Its limitation on modelling the residual stress of the strengthened glass results in several possible errors, i.e., a) overestimated delamination that will also underestimate the stress wave propagation speed. b) Inaccuracy in predicting the cracking sequence of the glass layer so that the contact duration is commonly overestimated. c) Limitations on modelling the realistic cracks in the loaded layer of the strengthened glass, although vertical crack in the bottom layer is captured correctly.

The proposed interfacial model can successfully capture the Mode I and Mode II dominant delamination behaviour in the vicinity of the impact point. In particular, the partial delamination in the bottom layer that is identical to the experimental observation can be located.

Overall, the proposed approach of FEM/DEM can reproduce the impact damage of laminated glass satisfactorily. It is predicted to have great potential to model the post breakage performance of laminated glass in three dimension manner if a more appropriate model can be sought to simulate the strengthened glass.

Acknowledgement

This work was supported by the National Key Research and Development Program of China [Grant No. 2017YFC0806100], the National Natural Science Foundation of China [Grant No. 51378308, 51508324] and the Science Research Plan of Shanghai Municipal Science and Technology Committee [Grant No. 17DZ1200306];

References

[1] Yuan Y, Tan PJ, Li Y. Dynamic structural response of laminated glass panels to blast loading. Composite Structures. 2017;182:579-89.

[2] Yuan Y, Xu C, Xu T, Sun Y, Liu B, Li Y. An analytical model for deformation and damage of rectangular laminated glass under low-velocity impact. Composite Structures. 2017;176:833-43.

[3] Del Linz P, Hooper PA, Arora H, Smith D, Pascoe L, Cormie D, et al. Reaction forces of laminated glass windows subject to blast loads. Composite Structures. 2015;131:193-206.

[4] Larcher M, Solomos G, Casadei F, Gebbeken N. Experimental and numerical investigations of

laminated glass subjected to blast loading. International Journal of Impact Engineering. 2012;39(1):42-50.

[5] Hidallana-Gamage HD, Thambiratnam DP, Perera NJ. Failure analysis of laminated glass panels subjected to blast loads. Engineering Failure Analysis. 2014;36:14-29.

[6] Chen X, Chan AHC, Yang J. Simulating the breakage of glass under hard body impact using the combined finite-discrete element method. Computers & Structures. 2016;177:56-68.

[7] Huang X-h, Yang J, Liu Q-f, Zhu J, Bai L, Wang F-l, et al. A simplified flange–lip model for distortional buckling of cold-formed steel channel-sections with stiffened web. International Journal of Mechanical Sciences. 2018;136:451-9.

[8] Liu Q-f, Feng G-l, Xia J, Yang J, Li L-y. Ionic transport features in concrete composites containing various shaped aggregates: a numerical study. Composite Structures. 2018;183:371-80.

[9] Sun X, Liu W, Chen W, Templeton D. Modeling and characterization of dynamic failure of borosilicate glass under compression/shear loading. International Journal of Impact Engineering. 2009;36(2):226-34.

[10] Zhao S, Dharani LR, Chai L, Barbat SD. Analysis of damage in laminated automotive glazing subjected to simulated head impact. Engineering Failure Analysis. 2006;13(4):582-97.

[11] Pyttel T, Liebertz H, Cai J. Failure criterion for laminated glass under impact loading and its application in finite element simulation. International Journal of Impact Engineering. 2011;38(4):252-63.

[12] Peng Y, Yang J, Deck C, Willinger R. Finite element modeling of crash test behavior for windshield laminated glass. International Journal of Impact Engineering. 2013;57:27-35.

[13] Pauw SD. Experimental and numerical study of impact on window glass fitted with safety window film: Ghent University; 2010.

[14] Potyondy DO, Cundall PA. A bonded-particle model for rock. International Journal of Rock Mechanics and Mining Sciences. 2004;41(8):1329-64.

[15] Tokunaga H, Kaizu K, Ikeda K, Kobori O. Impact Fracture Analysis of Thermally Tempered Glass by the Extended Distinct Element Method. Journal of Solid Mechanics and Materials Engineering. 2007;1(8):986-97.

[16] André D, Jebahi M, Iordanoff I, Charles J-l, Néauport J. Using the discrete element method to simulate brittle fracture in the indentation of a silica glass with a blunt indenter. Computer Methods in Applied Mechanics and Engineering. 2013;265:136-47.

[17] Zang MY, Lei Z, Wang SF. Investigation of impact fracture behavior of automobile laminated glass by 3D discrete element method. Computational Mechanics. 2007;41(1):73-83.

[18] Baraldi D, Cecchi A, Foraboschi P. Broken tempered laminated glass: Non-linear discrete element modeling. Composite Structures. 2016;140:278-95.

[19] Munjiza A. The Combined Finite-Discrete Element Method: John Wiley & Sons, Ltd; 2004.

[20] Chen X. Investigation on the impact damage of glass using the combined finite/discrete element method: University of Birmingham; 2013.

[21] Munjiza A, Lei Z, Divic V, Peros B. Fracture and fragmentation of thin shells using the combined finite–discrete element method. International Journal for Numerical Methods in Engineering. 2013;95(6):478–98.

[22] Butchart C, Overend M. Delamination in fractured laminated glass. Engineered transparency international conference at glasstec, 2012. p. 249 57.

[23] Froli M, Lani L. Adhesion, Creep and relaxation Properties of PVB in Laminated Safety Glass.

Glass Performance Days 2011. 2011:218-21.

[24] Munjiza A, Andrews KRF, White JK. Combined single and smeared crack model in combined finite-discrete element analysis. International Journal for Numerical Methods in Engineering. 1999;44(1):41-57.

[25] Munjiza A, Andrews KRF. NBS contact detection algorithm for bodies of similar size. International Journal for Numerical Methods in Engineering. 1998;43(1):131-49.

[26] Munjiza A, Andrews KRF. Penalty function method for combined finite–discrete element systems comprising large number of separate bodies. International Journal for Numerical Methods in Engineering. 2000;49(11):1377-96.

[27] Khajeh Mahabadi O. Investigating the influence of micro-scale heterogeneity and microstructure on the failure and mechanical behaviour of geomaterials. Toronto: University of Toronto; 2012.

[28] Xu J, Li Y, Ge D, Liu B, Zhu M. Experimental investigation on constitutive behavior of PVB under impact loading. International Journal of Impact Engineering. 2011;38(2–3):106-14.

[29] Yang Z, Zang M. Dynamic property and constitutive model of polyvinyl butaral material at high strain rates †. Polymers for Advanced Technologies. 2014;25(12):1377–85.

[30] Bower AF. Applied Mechanics of Solids: CRC Press; 2010.

[31] Pelfrene J, Dam SV, Paepegem WV. Numerical analysis of the peel test for characterisation of interfacial debonding in laminated glass. International Journal of Adhesion & Adhesives. 2015;62:146-53.

[32] Chen S, Zang M, Wang D, Zheng Z, Zhao C. Finite element modelling of impact damage in polyvinyl butyral laminated glass. Composite Structures. 2016;138:1-11.

[33] Van den Bosch M, Schreurs P, Geers M. An improved description of the exponential Xu and Needleman cohesive zone law for mixed-mode decohesion. Engineering Fracture Mechanics. 2006;73(9):1220-34.

[34] Dimitri R, Trullo M, De Lorenzis L, Zavarise G. Coupled cohesive zone models for mixed-mode fracture: A comparative study. Engineering Fracture Mechanics. 2015;148:145-79.

[35] Del Linz P, Liang X, Hooper PA, Wang LZ, Dear JP. An analytical solution for pre-crack behaviour of laminated glass under blast loading. Composite Structures. 2016;144:156-64.

[36] Wang X-e, Yang J, Liu Q-f, Zhang Y-m, Zhao C. A comparative study of numerical modelling techniques for the fracture of brittle materials with specific reference to glass. Engineering Structures. 2017;152:493-505.

[37] Kolluri M, Hoefnagels J, van Dommelen J, Geers M. Irreversible mixed mode interface delamination using a combined damage-plasticity cohesive zone enabling unloading. International Journal of Fracture. 2014;185(1-2):77-95.

[38] Flocker FW, Dharani LR. Modeling interply debonding in laminated architectural glass subject to low velocity impact. Structural Engineering & Mechanics. 1998;6(5):485-96.

[39] Xu X, Liu B, Li Y. Investigation on Dynamic Propagation Characteristics of In-Plane Cracks in PVB Laminated Glass Plates. Advances in Materials Science and Engineering. 2016;2016:13.

[40] Belis J, Delincé D, Callewaert D, Van Impe R, Depauw J. Plastic deformation of polymer interlayers during post-breakage behavior of laminated glass-partim 1: analytical approach. International Journal of Modern Physics B. 2009;22(31n32):5509-14.

[41] Grant PV, Cantwell WJ, McKenzie H, Corkhill P. The damage threshold of laminated glass structures. International Journal of Impact Engineering. 1998;21(9):737-46.